J. Fluid Mech. (2002), *vol.* 471, *pp.* 239–255.
DOI: 10.1017/S0022112002002239 Printed in the United Kingdom

Ekman effects in a rotating flow over bottom topography

By L. ZAVALA SANSÓN[1] AND G. J. F. VAN HEIJST[2]

[1]Department of Physical Oceanography, CICESE, Km 107 Carr. Tijuana-Ensenada, 22860, Ensenada BC, México

[2]Department of Physics, Eindhoven University of Technology, P.O. Box 513, 5600 MB Eindhoven, The Netherlands

(Received 19 June 2001 and in revised form 13 June 2002)

This paper presents a general two-dimensional model for rotating barotropic flows over topography. The model incorporates in a vorticity–stream function formulation both inviscid topography effects, associated with stretching and squeezing of fluid columns enforced by their motion over variable topography, and viscous effects, due to the Ekman boundary layer at the solid bottom. From the present formulation, conventional two-dimensional models can be recovered. The model is tested by means of laboratory experiments on homogeneous vortices encountering irregular topographies. The experimental observations are then compared with the corresponding numerical simulations based on the general model. The results suggest that such a formulation incorporates both inviscid and viscous topography effects correctly.

1. Introduction

Two-dimensional motion is commonly observed in laboratory experiments in a rotating fluid tank. When the rotation axis is aligned with gravity fluid motion is predominantly horizontal, i.e. in a plane perpendicular to the rotation axis. This phenomenon was predicted by S. S. Hough in 1897 (Gill 1982, p. 506) and by Proudman in 1916, and has been observed and reported in numerous experimental studies since the early works of Taylor (1923). In geophysical situations, nearly two-dimensional motion is also observed in large-scale flows, such as cold and/or warm eddies in the oceans, and tropical cyclones in the atmosphere. In these cases, the vertical direction is defined by the local component (perpendicular to the surface) of the planet's angular velocity. The two-dimensional character of such flows is due to the small ratio between the vertical and horizontal scales of motion. It has to be stressed, however, that the theoretical and experimental models developed in this study are strongly simplified models of large-scale flows affected by the Earth's rotation.

The essentially two-dimensional character of experimental and geophysical flows obviously does not strictly hold. For nearly geostrophic flow over weak topography variations, however, flow motion can be assumed predominantly two-dimensional, with small deviations due to topographic effects. There are two main effects associated with the presence of bottom topography: (*a*) stretching and squeezing of fluid columns enforced by their motion over variable topography, and (*b*) damping effects associated with the Ekman boundary layer at the solid bottom. Henceforth, they will be referred to as inviscid and viscous topography effects, respectively.

Inviscid topographic effects on a rotating homogeneous fluid layer can be described by the so-called barotropic non-divergent equations (see e.g. Grimshaw, Tang & Broutman 1994) or, for small topographic variations, by the quasi-geostrophic approximation (see e.g. Pedlosky 1987). In these models, the relative vorticity evolution is associated with stretching/squeezing of fluid columns as the flow experiences changes in depth.

A more complete description of the flow motion requires, however, the inclusion of bottom viscous effects, associated with the no-slip boundary condition at the solid bottom. In earlier studies some models were presented which incorporate the role of the Ekman layer in the geostrophic interior flow. Under the quasi-geostrophic formulation, bottom friction effects are usually included by adding a linear term in the relative vorticity equation. Wedemeyer (1964) derived a more complete model for spin-up in a rotating cylinder, which was later applied to the study of the spin-down of barotropic vortices by Kloosterziel & van Heijst (1992) and Maas (1993). Such a model, however, is limited to axisymmetric flows over a flat surface. Zavala Sansón & van Heijst (2000*a*, hereafter referred to as ZH00) report on a more general model, which satisfactorily describes the evolution of both axisymmetric and non-axisymmetric laboratory vortices. These studies used the linear Ekman condition over a flat bottom. In some other studies expansions in the Rossby number were carried out in order to obtain a nonlinear Ekman condition (see e.g. Hart 1995, 2000). One of the main results obtained with such formulations is that cyclones decay faster than anticyclones. This can also be deduced, however, using the linear Ekman condition and retaining the nonlinear Ekman terms in the evolution equations, as shown by ZH00 and Zavala Sansón, van Heijst & Backx (2001). Besides, using the nonlinear Ekman condition leads to complicated equations that are difficult to manipulate, which obscures the physical processes involved.

This paper presents a general two-dimensional model for barotropic flow including inviscid and viscous topography effects. The analysis described here incorporates both effects in a two-dimensional model, written in a vorticity–stream function formulation, which basically consists of an evolution equation for the vertical component of the relative vorticity. The crucial step in the derivation consists of introducing stretching/squeezing effects (due to variable topography) together with the well-known linear Ekman condition (the vertical velocity induced by the Ekman layer at the bottom), obtained by integrating the continuity equation in the vertical direction. Then, the nonlinear terms associated with the Ekman effects in the resultant vorticity evolution equation are retained (a similar procedure was applied in ZH00 in order to include only Ekman friction, linear and nonlinear, produced by a flat bottom). The inclusion of nonlinear Ekman terms in the vorticity equation, in addition to the well-known linear Ekman term, is the main characteristic of the physical model. This approximation is valid only for relatively smooth topographies, where the Ekman condition can be used. In addition, the Rossby number, which indicates the relative importance of rotation effects, is required to be small to moderate ($O(1)$ or less). The present formulation can be reduced to well-known conventional models when bottom friction and/or variable topography are ignored.

In order to validate the general two-dimensional model, laboratory experiments on barotropic vortices over different topographies were compared with numerical simulations based on this approximation. The principal aim of the simulations is to investigate to what extent the two-dimensional model including topographic effects (inviscid and viscous) is able to reproduce the main characteristics of the experimentally observed flow evolutions, therefore capturing the basic physical mechanisms in

the problem. For this purpose, the experimental results of Vosbeek (1998) on the evolution of a tripolar vortex affected by a weak parabolic topography (equivalent to the so-called γ-plane) are considered. It is found that her quantitative and qualitative measurements are well-reproduced by numerical simulations based on the extended formulation. Furthermore, it is shown that the model is clearly superior to the conventional barotropic non-divergent equations, which do not include bottom friction, and to the classical quasi-geostrophic approximation with linear Ekman damping. In addition, an example of a vortex encountering a topographic ridge is presented. This problem was studied by means of laboratory experiments and numerical simulations by Zavala Sansón (2002). Although the ridge is a more complicated topography, the general model is able to reproduce qualitatively the main experimental results.

The paper is organized as follows. The extended two-dimensional model is derived in § 2, and it is shown that this formulation can be reduced to other conventional two-dimensional approximations. In § 3 the model is tested by means of numerical simulations of laboratory experiments in a rotating tank. In § 4 some final remarks are presented.

2. Ekman friction over variable topography

2.1. *The model*

Here the extended model with inviscid and viscous topography effects is derived (a similar procedure was followed in ZH00 for including only viscous effects over a flat bottom). Consider a homogeneous fluid layer in a Cartesian coordinate system, rotating with angular frequency Ω about the z-axis. In the vertical direction (aligned with the gravitational acceleration), the motion is confined to

$$h_B \leqslant z \leqslant h + h_B, \tag{2.1}$$

where $h(x, y, t)$ is the layer depth and $h_B(x, y)$ describes the spatially variable bottom topography. Note that h contains the free-surface elevation associated with the flow itself, which may be time-dependent. The horizontal velocity components $\boldsymbol{u} = (u, v)$ are considered z-independent, and the hydrostatic balance is assumed to apply in the vertical direction. As usual, the horizontal pressure gradients are eliminated by taking the curl of the momentum equation, yielding

$$\frac{\partial \omega}{\partial t} + u\frac{\partial \omega}{\partial x} + v\frac{\partial \omega}{\partial y} + \left(\frac{\partial u}{\partial x} + \frac{\partial v}{\partial y}\right)(\omega + f) = \nu \nabla^2 \omega, \tag{2.2}$$

where $\omega = \partial v/\partial x - \partial u/\partial y$ is the relative vorticity, $f = 2\Omega$ is the Coriolis parameter with Ω the rotation rate of the system, t is the time, ν is the kinematic viscosity and $\nabla^2 = \partial^2/\partial x^2 + \partial^2/\partial y^2$ is the horizontal Laplacian operator. The continuity equation is

$$\frac{\partial u}{\partial x} + \frac{\partial v}{\partial y} + \frac{\partial w}{\partial z} = 0, \tag{2.3}$$

where w is the vertical velocity component.

Adequate expressions to substitute the horizontal velocity components (u and v) and the horizontal divergence ($\partial u/\partial x + \partial v/\partial y$) in (2.2) are obtained by integrating the continuity equation over the fluid depth, i.e. from $z = h_B$ to $z = h + h_B$. This integration, which is possible since u and v have been assumed z-independent, yields

$$\left(\frac{\partial u}{\partial x} + \frac{\partial v}{\partial y}\right) h = -(w|_{z=h+h_B} - w|_{z=h_B}). \tag{2.4}$$

Ignoring wind stress, the vertical velocity on the free surface is given by the kinematic condition

$$w|_{z=h+h_B} = \frac{\mathrm{D}}{\mathrm{D}t}(h + h_B), \tag{2.5}$$

with $\mathrm{D}/\mathrm{D}t$ the material derivative.

For low-Rossby-number flows, the vertical velocity induced by the thin Ekman layer at the bottom is given by the so-called Ekman condition, which states that this velocity is proportional to the relative vorticity of the interior flow outside the Ekman layer. For variable bottom topography the Ekman condition can be expressed as (see e.g. Pedlosky 1987)

$$w|_{z=h_B} = \boldsymbol{u} \cdot \nabla h_B + \tfrac{1}{2}\delta_E \omega, \tag{2.6}$$

where the thickness of the Ekman layer is

$$\delta_E = \left(\frac{2\nu}{f}\right)^{1/2}. \tag{2.7}$$

Note that the first part of the Ekman condition, $\boldsymbol{u} \cdot \nabla h_B$, expresses the vertical velocity induced by the shape of the topography (see e.g. Charney & Eliassen 1949; Huppert & Bryan 1976), which is zero for a flat bottom.

With (2.5) and (2.6) the horizontal divergence in (2.4) may be written as

$$\frac{\partial u}{\partial x} + \frac{\partial v}{\partial y} = -\frac{1}{h}\frac{\mathrm{D}h}{\mathrm{D}t} + \frac{\delta_E}{2h}\omega. \tag{2.8}$$

This expression states that the horizontal divergence is caused by changes in the fluid depth associated with free-surface variations and topography effects (both included in h) and by the vertical velocity induced by the Ekman layer at the bottom. Neglecting the temporal variations of the free-surface elevation, the time derivative can be filtered out, i.e. $h \equiv h(x, y)$, and (2.8) then becomes

$$\frac{\partial u}{\partial x} + \frac{\partial v}{\partial y} = -\frac{1}{h}\left(u\frac{\partial h}{\partial x} + v\frac{\partial h}{\partial y}\right) + \frac{\delta_E}{2h}\omega. \tag{2.9}$$

Note that for the flat bottom case ($h = H =$ constant) $\delta_E/H = E^{1/2}$, with $E = 2\nu/fH^2$ the Ekman number. More importantly, note that this expression for the horizontal divergence also accommodates a flat bottom and spatially variable surface topography. In such a case, the upper boundary condition is simply $w|_{z=h} = u\partial h/\partial x + v\partial h/\partial y$, whilst the lower boundary condition is $w|_{z=0} = \frac{1}{2}\delta_E \omega$.

Substitution of (2.9) in (2.2) yields, after some manipulations,

$$\frac{\partial \omega}{\partial t} + hu\frac{\partial q}{\partial x} + hv\frac{\partial q}{\partial y} = \nu\nabla^2\omega - \frac{\delta_E}{2h}\omega(\omega + f), \tag{2.10}$$

where

$$q = \frac{\omega + f}{h} \tag{2.11}$$

is the potential vorticity.

Expressions for u and v are obtained by rewriting (2.9) as

$$\frac{\partial}{\partial x}(hu - \tfrac{1}{2}\delta_E v) + \frac{\partial}{\partial y}(hv + \tfrac{1}{2}\delta_E u) = 0 \tag{2.12}$$

and by defining a function ψ such that

$$hu - \tfrac{1}{2}\delta_E v = \frac{\partial \psi}{\partial y}, \tag{2.13}$$

$$hv + \tfrac{1}{2}\delta_E u = -\frac{\partial \psi}{\partial x}. \tag{2.14}$$

From these equations, the corresponding expressions for the velocities in terms of the stream function are obtained:

$$u = \frac{1}{1 + (\delta_E/2h)^2} \frac{1}{h} \left(\frac{\partial \psi}{\partial y} - \frac{\delta_E}{2h} \frac{\partial \psi}{\partial x} \right), \tag{2.15}$$

$$v = \frac{1}{1 + (\delta_E/2h)^2} \frac{1}{h} \left(-\frac{\partial \psi}{\partial x} - \frac{\delta_E}{2h} \frac{\partial \psi}{\partial y} \right). \tag{2.16}$$

Assuming, however, that $(\delta_E/2h)^2 \ll 1$, i.e. that the Ekman layer thickness is always much smaller than the fluid depth, the horizontal velocities can be simplified as follows:

$$u = \frac{1}{h} \left(\frac{\partial \psi}{\partial y} - \frac{\delta_E}{2h} \frac{\partial \psi}{\partial x} \right), \tag{2.17}$$

$$v = \frac{1}{h} \left(-\frac{\partial \psi}{\partial x} - \frac{\delta_E}{2h} \frac{\partial \psi}{\partial y} \right). \tag{2.18}$$

By inserting (2.17) and (2.18) in the definition of the relative vorticity ($\omega = \partial v/\partial x - \partial u/\partial y$) it is verified that

$$\omega = -\frac{1}{h}\nabla^2 \psi + \frac{1}{h^2} \nabla h \cdot \nabla \psi + \frac{\delta_E}{2h} \frac{2}{h^2} J(h, \psi), \tag{2.19}$$

where J is the Jacobian operator. Finally, the evolution equation for the relative vorticity is obtained by substituting (2.17) and (2.18) in (2.10):

$$\frac{\partial \omega}{\partial t} + J(q, \psi) - \frac{\delta_E}{2h} \nabla \psi \cdot \nabla q = \nu \nabla^2 \omega - \frac{\delta_E}{2h} \omega(\omega + f). \tag{2.20}$$

The horizontal velocities (2.17) and (2.18), the modified Poisson equation (2.19) and the vorticity evolution equation (2.20), represent the ω–ψ formulation of the two-dimensional model for a rotating fluid over variable topography, including the Ekman damping.

Note that the Ekman terms are proportional to the x, y-dependent factor $\delta_E/2h(x, y)$. Advection effects driven by the Ekman layer are represented by the third term on the left-hand side of (2.20), while the Ekman terms on the right-hand side represent stretching effects associated with the Ekman suction or blowing. Obviously, Ekman effects are enhanced in shallow layers, i.e. where h decreases.

2.2. *Summary of two-dimensional models*

The general two-dimensional model derived in the previous subsection can be reduced to some other approximations as follows.

(i) *Purely two-dimensional model*

First, consider a flat bottom ($h = H =$ constant, $\nabla h = 0$) and no bottom friction ($\delta_E = 0$, see figure 1*a*). Defining the stream function as

$$\psi^{(*)} = \frac{1}{H} \psi, \tag{2.21}$$

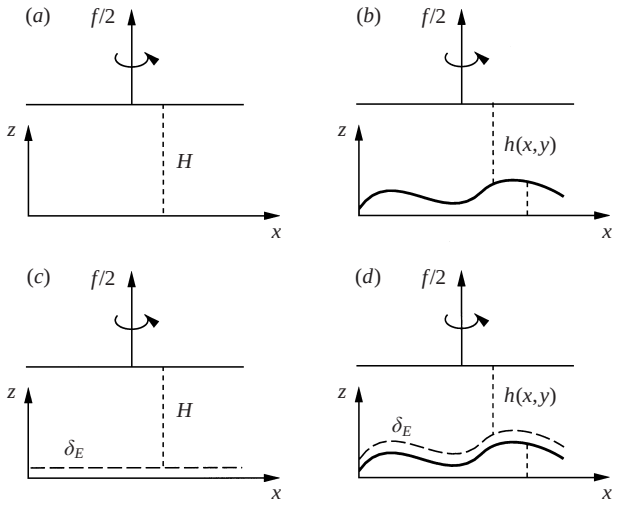

FIGURE 1. Summary of two-dimensional models in a rotating system with and without topography effects: (*a*) purely two-dimensional model, (*b*) barotropic non-divergent model, (*c*) two-dimensional model with Ekman friction over a flat bottom, (*d*) general two-dimensional model.

the corresponding equations become

$$u = \frac{\partial \psi^{(*)}}{\partial y}, \tag{2.22}$$

$$v = -\frac{\partial \psi^{(*)}}{\partial x}, \tag{2.23}$$

$$\omega = -\nabla^2 \psi^{(*)}, \tag{2.24}$$

$$\frac{\partial \omega}{\partial t} + J(\omega, \psi^{(*)}) = \nu \nabla^2 \omega, \tag{2.25}$$

which is the well-known two-dimensional model without topography effects.

(ii) *Barotropic non-divergent model*

For arbitrary topographic variations $h = h(x, y)$ and ignoring bottom friction ($\delta_E = 0$, see figure 1*b*) the model reduces to

$$u = \frac{1}{h}\frac{\partial \psi}{\partial y}, \tag{2.26}$$

$$v = -\frac{1}{h}\frac{\partial \psi}{\partial x}, \tag{2.27}$$

$$\omega = -\frac{1}{h}\nabla^2 \psi + \frac{1}{h^2}\nabla h \cdot \nabla \psi, \tag{2.28}$$

$$\frac{\partial \omega}{\partial t} + J(q, \psi) = \nu \nabla^2 \omega. \tag{2.29}$$

Note that in this case, it is not necessary to redefine the stream function. For further details see e.g. Grimshaw *et al.* (1994). This model may be used to describe inviscid topography effects on experimental vortices when the duration of the experiments is

shorter than the Ekman period (see e.g. Zavala Sansón & van Heijst 2000*b*).

(iii) *Two-dimensional model with Ekman friction over a flat bottom*

For a flat bottom ($h = H =$ constant, $\nabla h = 0$) but now considering bottom friction ($\delta_E \neq 0$, $\delta_E/H = E^{1/2}$, see figure 1*c*), the stream function (2.21) can again be used, and the equations transform to

$$u = \frac{\partial \psi^{(*)}}{\partial y} - \tfrac{1}{2}E^{1/2}\frac{\partial \psi^{(*)}}{\partial x}, \tag{2.30}$$

$$v = -\frac{\partial \psi^{(*)}}{\partial x} - \tfrac{1}{2}E^{1/2}\frac{\partial \psi^{(*)}}{\partial y}, \tag{2.31}$$

$$\omega = -\nabla^2 \psi^{(*)}, \tag{2.32}$$

$$\frac{\partial \omega}{\partial t} + J(\omega, \psi^{(*)}) - \tfrac{1}{2}E^{1/2}\nabla\psi^{(*)} \cdot \nabla\omega = \nu\nabla^2\omega - \tfrac{1}{2}E^{1/2}\omega(\omega + f). \tag{2.33}$$

This model, in which the Ekman effects are represented by the terms proportional to $E^{1/2}$, was derived in ZH00. The conventional two-dimensional model with Ekman damping (used in many other studies) does not consider the nonlinear Ekman effects, but only the linear stretching term $E^{1/2}\omega f/2$. It was demonstrated in ZH00 that the description of barotropic vortices in laboratory experiments (during periods comparable to the Ekman timescale) is significantly improved when nonlinear Ekman terms are considered in the corresponding numerical simulations.

3. Experiments and simulations

The model of two-dimensional flow over spatially varying topography with Ekman effects given by (2.17), (2.18), (2.19) and (2.20) is tested by means of laboratory experiments and numerical simulations. A similar procedure was followed by ZH00 in order to evaluate the model given by (2.30)–(2.33), which includes Ekman effects on a flat bottom, i.e. with no topographic variations. Here, laboratory experiments on barotropic vortices over variable topography for times of the order of the Ekman period, are compared with the corresponding numerical simulations based on the general model. In order to do this, it is useful to perform experiments from which both qualitative and quantitative measurements can be taken. As shown in ZH00, quantitative measurements of vortices over a flat bottom are relatively easy to obtain. Over variable topography, however, this is not usually the case because of experimental difficulties and/or complicated flow behaviours. For this reason, the evolution of a tripolar vortex in the presence of a parabolic surface, presented by Vosbeek (1998), is examined first. Due to the relatively small depth variations in that experiment, the author was able to obtain quantitative measurements, namely the peak vorticity in the vortex core, which can be compared with simulations using model (2.17)–(2.20). Then, the qualitative behaviour of a non-isolated cyclonic vortex over a topographic ridge is observed and compared with the evolution of passive tracers from numerical simulations. In this case the bottom variations are much more dramatic, which produces a complicated distortion of the vortex.

It is important to emphasize that, in order to appreciate bottom friction effects, the duration of the experiments and simulations must be of the order of the Ekman

period, defined as

$$T_E = \frac{2}{fE^{1/2}} = \left(\frac{2}{fv}\right)^{1/2} H_m, \tag{3.1}$$

where H_m is the average depth over the topography. By taking the kinematic viscosity as $v \sim 0.01\,\mathrm{m^2\,s^{-1}}$, the Coriolis parameter $f \sim 1\,\mathrm{s^{-1}}$, and the mean depth $H_m \sim 15\,\mathrm{cm}$, the Ekman period is 200 s, approximately.

The numerical simulations were performed by using a finite differences code. The relation between the relative vorticity and the stream function, (2.19), is solved by using a multigrid method from a NAG routine. This procedure has already been successfully used in Zavala Sansón & van Heijst (2000*b*), where the barotropic non-divergent equations were solved. For further details on the numerical scheme see also van Geffen (1998), who used a similar method for including inviscid topography effects.

3.1. *Vortices on a γ-plane*

It has been shown in previous experimental studies that vortices created over a flat bottom and off the centre of a rotating tank experience changes in depth associated with the parabolic surface (see e.g. Velasco Fuentes, van Heijst & Lipzig 1996; Vosbeek 1998). In geophysical fluid dynamics, this effect is usually referred to as the γ-effect, which represents an approximation of the Coriolis parameter near the poles, where its spatial variations can be represented by a quadratic term. The γ-effect is usually ignored in experiments in which changes in depth due to bottom topography are greater than those associated with the free surface (e.g. Zavala Sansón & van Heijst 2000*b*). For a flat bottom, however, such an effect might be important in the flow evolution. Here, the experimental results of Vosbeek (1998) concerning the behaviour of tripolar vortices under the influence of the γ-effect are considered. Then a typical experiment is numerically simulated by using the extended model, which can also be applied for flows over a flat bottom and a spatially variable surface, as mentioned in § 2.

The cyclonic structures studied by Vosbeek (1998) are vortices consisting of a cyclonic core surrounded by an annulus of oppositely signed vorticity in such a way that the vortex contains zero net vorticity. Such isolated vortices are easily created by placing a small, bottomless cylinder in the tank, stirring the fluid in the cylinder, and then removing it, thus releasing the vortex in the ambient solidly rotating fluid (see e.g. Carnevale, Kloosterziel & van Heijst 1991). For the flat-bottom case, typical radial distributions of the vorticity and azimuthal velocity are

$$\omega_{stir}(r) = \omega_0 \left(1 - \frac{\alpha}{2}\left(\frac{r}{R}\right)^{\alpha}\right) \exp\left(-\left(\frac{r}{R}\right)^{\alpha}\right), \tag{3.2}$$

$$v_{stir}(r) = \frac{\omega_0 r}{2} \exp\left(-\left(\frac{r}{R}\right)^{\alpha}\right), \tag{3.3}$$

where ω_0 is the peak vorticity, R a horizontal length scale, r the radial distance to the centre of the vortex, and α a parameter controlling the shape of the radial profile. Isolated cyclonic vortices over a flat bottom are often observed to evolve towards a tripolar structure, formed by a cyclonic core with two anticyclonic satellites. The tripole rotates in cyclonic direction while slowly decaying (van Heijst, Kloosterziel & Williams 1991; ZH00). When the vortex is created off the centre of the rotating tank, the tripolar structure is again formed, but now showing an asymmetric behaviour due to the γ-effect, which induces the vortex to move towards the centre of the tank.

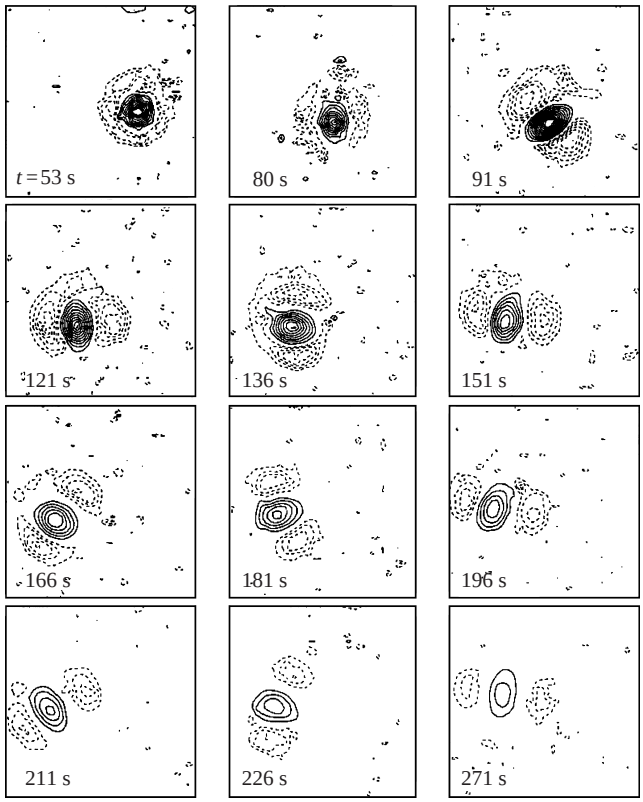

FIGURE 2. Sequence of vorticity contours of a tripolar vortex in a laboratory experiment taken from Vosbeek (1998). The Ekman period is $T_E = 211$ s. Positive (negative) contours are plotted with solid (dashed) lines. Contours are drawn for $\omega = -0.6, -0.5, \ldots, -0.1, 0.2, 0.4, \ldots, 2.4$. The measured vortex parameters are $\alpha = 1.8$, $R = 7.5$ cm, and $\omega_0 = 5\,\mathrm{s}^{-1}$. The domain shown is a 80 cm $\times$ 80 cm square.

Figure 2 shows a sequence of vorticity contours of a tripolar vortex in a laboratory experiment under the influence of the parabolic surface. The vorticity (and velocity) fields were obtained by means of passive particles floating over the free surface, from which their velocities can be obtained, and fitting the experimental data to (3.3). The experiment was performed in a rotating tank with horizontal dimensions 150 cm $\times$ 100 cm. The domain shown is a square of 80 cm $\times$ 80 cm, centred at the axis of rotation. The tank is rotated in the anticlockwise direction at a constant rate of $\Omega = 0.61\,\mathrm{s}^{-1}$, which corresponds to a Coriolis parameter $f = 2\Omega = 1.22\,\mathrm{s}^{-1}$. Filled with fresh tap water, the tank is set at the specified constant rotation about 30 min before the start of the experiment in order to ensure that the fluid has reached a state of solid-body rotation. The parabolic shape of the surface is given by

$$h(r) = H + \frac{f^2 r^2}{8g}, \tag{3.4}$$

where $H = 16$ cm is the fluid depth at the rotation axis, g the acceleration due to gravity and r the distance from the rotation axis. Note that depth variations are very small compared with H; for instance at $r = 40$ cm the elevation of the surface is only 0.3 cm. For this reason, and considering that the vortex is rather intense, topographic waves are very weak, and therefore not relevant to the flow evolution.

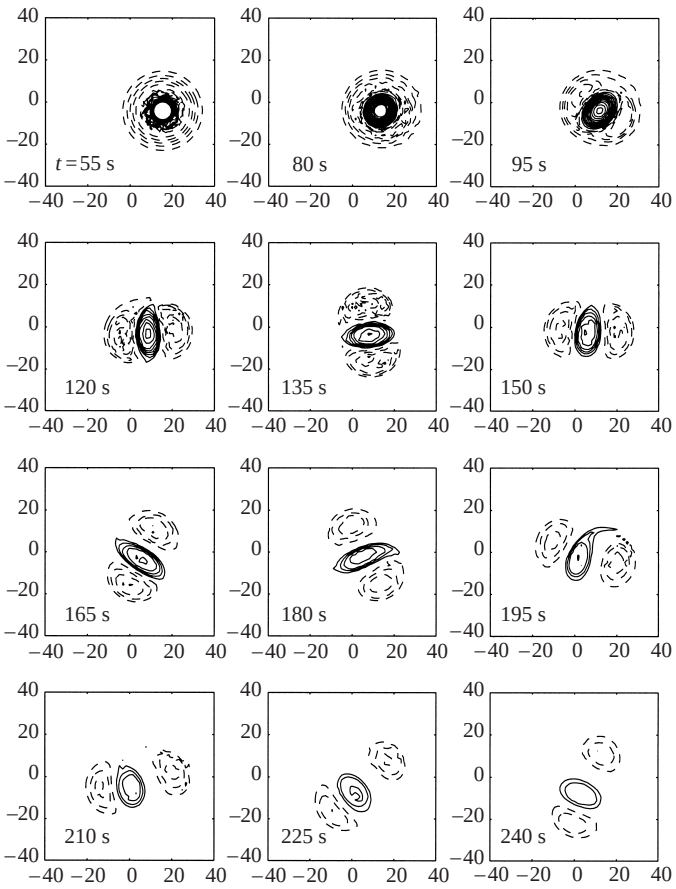

FIGURE 3. Sequence of vorticity contours of a tripolar vortex in a numerical simulation based on the extended model, and using the same flow parameters and contours as in the experiment shown in figure 2. All panels except the last one are comparable with that experiment.

The Ekman period is about 210 s. Taking the origin (0, 0) at the centre of the tank, an isolated vortex was created approximately at (20 cm, 0 cm), i.e. at the right-hand part of the domain. The first plot was taken 53 s after the creation of the cyclone. At this time, the measured vortex parameters are $\alpha = 1.8$, $R = 7.5$ cm, and $\omega_0 = 5\,\mathrm{s}^{-1}$, whilst the position of its centre is approximately (16 cm, −4 cm). The Rossby number ϵ associated with the vortex can be defined proportional to $v_{stir}(R)/fR \approx 0.75$. Although the vortex is initially intense ($\epsilon \sim O(1)$) it gradually decays due to bottom friction and to lateral diffusion of momentum. In a similar fashion as in the flat-bottom case, the vortex evolves towards a tripolar structure, formed by a cyclonic core with two anticyclonic satellites, which eventually rotates in a cyclonic direction (see van Heijst *et al.* 1991). The parabolic surface, however, induces the tripole to drift towards the centre of the tank. Velasco Fuentes *et al.* (1996) showed that this behaviour is due to the alternating intensification of the negative satellites, which pair with the cyclonic core as the tripole rotates.

Figure 3 shows the evolution of an isolated vortex calculated numerically with model (2.17)–(2.20) and using the same experimental parameters. The initial vorticity distribution, given by (3.2), was randomly perturbed using a similar method to Orlandi

& van Heijst (1992), who studied numerically the tripole evolution over a flat bottom. A perturbation of this type leads to the formation of the tripolar vortex structure. Relative vorticity contours are shown for similar times as the experiment (except the last panel), during a timespan of approximately $1.15T_E$. This simulation shows that the main features of the experimental results in figure 2 are well-reproduced, namely the tripole formation at $t = 90$ s and the anticyclonic rotation of the whole structure during the experiment. From the number of contours at each time it can be observed that the numerical vortex decays at a very similar rate as in the experiment (the quantitative vortex decay is further examined below). It must be emphasized that the most important result is not the agreement between the experiment and simulation, but that such an agreement is observed for more than one Ekman period. Perhaps the main difference is that the experimental vortex drifts slightly more to the left of the domain, whilst the numerical vortex remains at the centre. The reason for this behaviour might be related to a small impulse to the vortex when releasing the cylinder within which it was created (P. Vosbeek, personal communication).

Since topographic variations are very small in this experiment, one may wonder whether the conventional quasi-geostrophic approximation could be sufficient to obtain a similar result as with the extended model. The answer is no. The quasi-geostrophic formulation is obtained by writing the depth field as $h = H(1 - h_B/H)$, and by considering small topographic variations, $h_B/H \ll 1$. Thus the potential vorticity can be approximated as

$$q = \frac{\omega + f}{H(1 - h_B/H)}$$

$$\sim \frac{\omega + f}{H}(1 + h_B/H + \cdots). \tag{3.5}$$

Neglecting terms $O(\omega h_B/H)$, $O(f h_B^2/H^2)$ and higher, the potential vorticity is reduced to $q \sim (f + \omega + f h_B/H)/H$. Omitting nonlinear Ekman terms in (2.20), and defining the horizontal velocities as in the two-dimensional case (equations (2.22) and (2.23)), the vorticity equation becomes

$$\frac{\partial \omega}{\partial t} + J(q_G, \psi^{(*)}) = \nu \nabla^2 \omega - \tfrac{1}{2} E^{1/2} f \omega, \tag{3.6}$$

where the quasi-geostrophic potential vorticity is defined as

$$q_G = \omega + f h_B/H. \tag{3.7}$$

This approximation contains only the linear bottom friction term, whilst topographic variations are contained in the potential vorticity definition.

Figure 4 shows the vorticity contours of an identical vortex during the same time-span shown in figure 3, from a numerical simulation based on the quasi-geostrophic model (3.6). The differences with the new model are remarkable, since the tripolar vortex has not even developed, and the vortex just drifts towards the centre of the domain. This is a clear indication of the importance of nonlinear Ekman terms. In order to verify this assertion, an additional simulation based on the extended model (2.20) but now using only the linear Ekman effect was performed (not shown here). As expected, the result is almost identical to the quasi-geostrophic simulation.

A more quantitative test consists of comparing the peak vorticity decay in the experiment and the simulations. Figure 5 shows the experimental values measured by Vosbeek (1998) and the calculated results from simulations based on the extended and the quasi-geostrophic models. It is observed that although the new formulation slightly

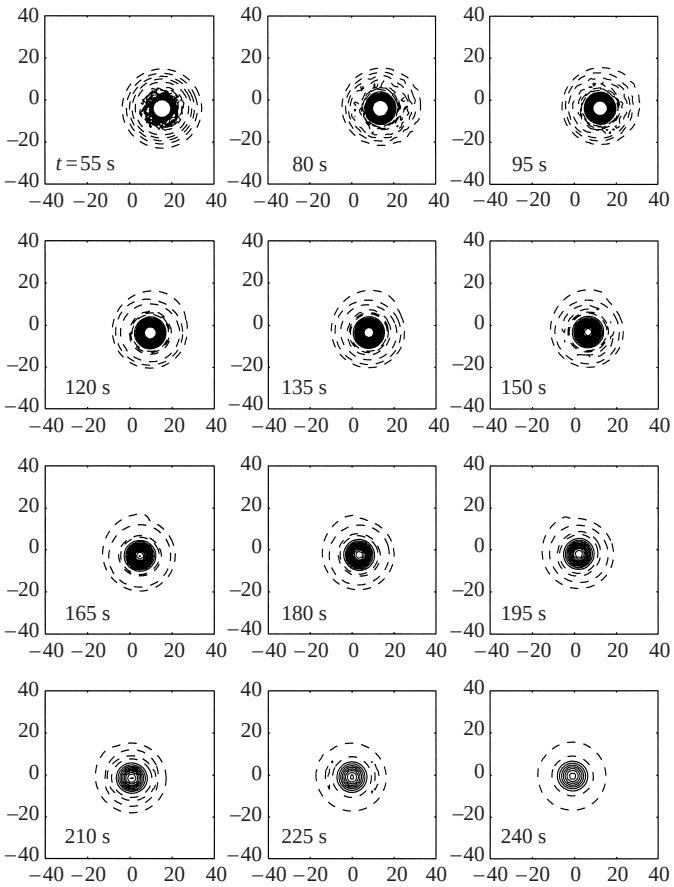

FIGURE 4. Sequence of vorticity contours of a tripolar vortex in a numerical simulation based on the quasi-geostrophic model, using the same flow parameters and contours as in figure 2.

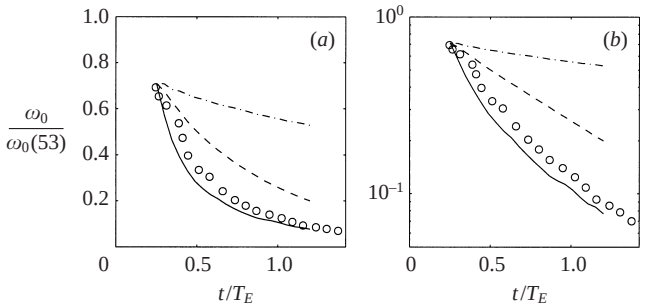

FIGURE 5. (*a*) Time evolution of the tripole's peak vorticity. Circles denote measurements from the experiment shown in figure 2. The solid lines denote the numerical simulation using the extended model, dashed lines represent the quasi-geostrophic simulation, and dash-dotted lines denote the numerical simulation without Ekman effects. (*b*) The same result in a logarithmic scale.

overestimates the peak vorticity decay, it gives a much better result than the quasi-geostrophic approximation, which decays exponentially, as shown in figure 5(*b*). The ability of the numerical solution to represent quantitatively the experimental result is remarkable given that the duration of the simulation was greater than the Ekman

timescale, which is much longer than the rotation period of the system. The decay in the absence of bottom friction, calculated with equations (2.26)–(2.29), is also shown.

3.2. *Vortices over a topographic ridge*

In this section, the qualitative evolution of cyclonic vortices encountering a topographic ridge is presented. Here it is shown that, even though the ridge is a more pronounced topography than the parabolic surface, the experimental vortex evolution is numerically well-simulated by using the general two-dimensional model. The vortex–ridge interaction problem was studied in detail by Zavala Sansón (2002), who reported laboratory experiments and numerical simulations. For further details on the experimental procedures and results the reader is referred to that study.

In the experiment presented here, the Coriolis parameter was $f = 1\,\mathrm{s}^{-1}$, whilst the maximum depth of the rectangular tank (with the same dimensions as in previous example, 150 cm × 100 cm) was $H = 21$ cm. A topographic ridge with an isosceles-triangular cross-section was fixed on the otherwise flat bottom of the tank. The ridge height was $h_r = 3$ cm and the (half-) width $W = 10$ cm. The top of the ridge is at $x = 75$ cm and the edges are at $x_{left} = 75 - W$, and $x_{right} = 75 + W$ cm. In contrast with the γ-plane experiment, it is anticipated here that changes in depth due to the ridge are much more important than the effects of the parabolic free surface, and therefore the latter will be ignored.

For these experiments cyclonic sink vortices were used. The sink vortices have a single-signed vorticity and are hence non-isolated. This type of vortex is produced by locally syphoning a fixed amount of fluid, during a certain period of time, through a thin perforated tube (for further details, see e.g. Hopfinger & van Heijst 1993). For the flat-bottom case, typical radial distributions of the vorticity and azimuthal velocity are

$$\omega_{sink}(r) = \omega_0 \exp\left(\frac{-r^2}{R^2}\right), \tag{3.8}$$

$$v_{sink}(r) = \frac{R^2\omega_0}{2r}\left(1 - \exp + \left(\frac{-r^2}{R^2}\right)\right), \tag{3.9}$$

where ω_0 is the peak vorticity, R a horizontal length scale, and r the radial distance to the centre of the vortex. As mentioned before, such structures have a single-signed vorticity and are hence non-isolated, which allows the vortex to experience the influence of the ridge, even when it is initially placed at a large distance (compared with the vortex size) from the topographic feature.

Figure 6 presents the evolution of a sink vortex (visualized with dark dye) encountering the ridge. The cyclone is created at $(x_0, y_0) \approx (50\,\mathrm{cm}, 20\,\mathrm{cm})$ and its initial parameters are approximately $\omega_0 = 4\,\mathrm{s}^{-1}$ and $R = 2.5$ cm, which gives an initial Rossby number of $v_{sink}(R)/fR \approx 1.2$. These parameters are obtained by repeating the experiment with passive particles floating over the free surface, and fitting the experimental data to (3.9) (analogous to the tripole experiment, see also e.g. ZH00). The circle indicates the approximate size and position of the vortex at $t = 0$ s (i.e. when the forcing was stopped). Dashed lines show the edges of the ridge, which is centred at $x = 75$ cm. The figure shows the vortex evolution during a strong interaction: the vortex approaches the ridge, climbs the ascending slope, and crosses to the other side, now moving in the opposite direction. At $t = 150$ s, the vortex is at the top of the ridge and the shape becomes slightly elliptical, with the major axis perpendicular to the isobaths. When the vortex has crossed the ridge it is strongly

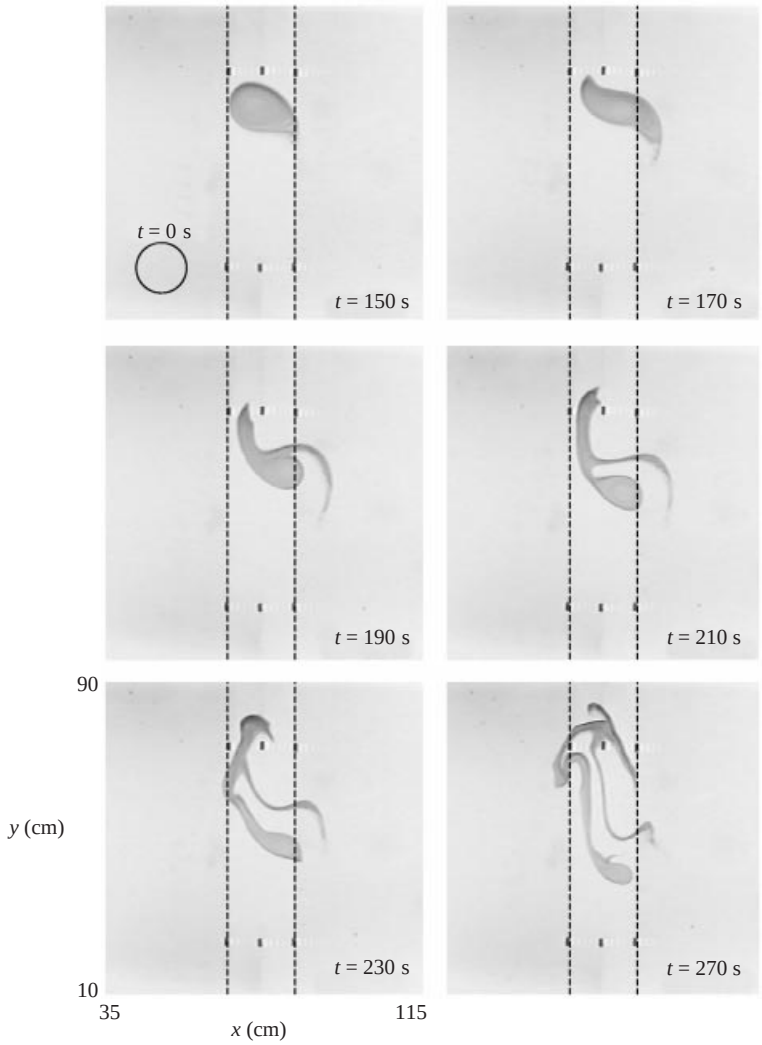

FIGURE 6. Top view photographs showing the evolution of a vortex during a strong interaction with a topographic ridge. The parameters of the ridge are $h_r = 3\,\text{cm}$ and $W = 10\,\text{cm}$.

deformed and the direction of motion is reversed, i.e. the vortex now moves in the new local northwestern direction, imposed by the opposite slope, trying to cross back over the ridge again. During this process part of its mass has been lost at the left-hand side ($t = 190$–$210\,\text{s}$). The formation of a thin filament at the right-hand side of the vortex at $t = 190\,\text{s}$ is also very clear. In the final stages of the experiment the vortex has been dissipated and the dyed fluid forms a long tendril distributed along the ridge ($t = 230$–$270\,\text{s}$). Note that using $H_m \approx 20\,\text{cm}$, $\nu = 0.01\,\text{cm}^2\,\text{s}^{-1}$ and $f = 1\,\text{s}^{-1}$ in expression (3.1), gives the Ekman period of approximately $T_E \approx 280\,\text{s}$, which indicates that the experimental vortex is affected by Ekman damping effects.

The elliptical shape of the vortex when it crosses the top of the ridge is associated with the topographic Rossby radiation over the slopes of the topography. Zavala Sansón (2001) showed that this process is due to the formation of opposite circulation cells (i.e. anticyclonic) formed over the ridge, due to squeezing effects (not visible

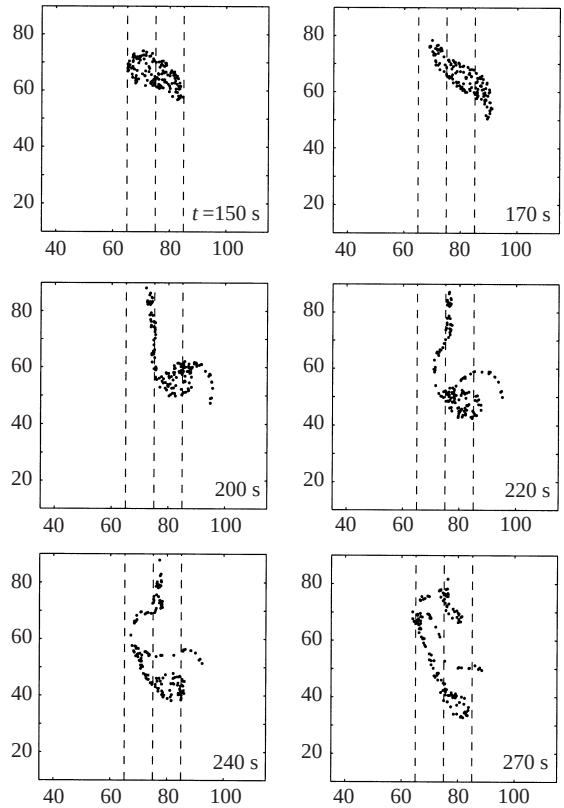

FIGURE 7. Calculated evolution of 500 tracers initially placed in a circle of radius 7 cm and centred at the vortex core, showing a strong interaction comparable with the experiment in figure 6. The flow parameters are: $H = 21$ cm, $R = 2.5$ cm, $\omega_0 = 3\,\mathrm{s}^{-1}$ and $(x_0, y_0) = (50\,\mathrm{cm}, 20\,\mathrm{cm})$.

from the presented photographs). Then, the combination of these circulation patterns produces the subsequent vortex deformation and formation of filaments. In contrast with the parabolic-free-surface case, changes in depth associated with the ridge are important enough to produce topographic radiation.

The qualitative experimental results can be numerically reproduced, as shown in figure 7, where the calculated evolution of 500 passive tracers initially placed around the vortex core is presented. The tracers are randomly distributed, and their evolution is equivalent to the dye distribution in the laboratory experiments. It is remarkable that the complicated dye distributions in the experiments are well-reproduced during the simulation, namely the initial deformation of the vortex ($t = 150$ and 170 s), and the formation of long filaments as the vortex experiences the opposite slope of the ridge ($t = 200$ and 220 s). Even for later times ($t = 240$ and 270 s) the dye evolution is quite similar. This figure is clear evidence that the flow remains nearly two-dimensional, and that (2.19)–(2.10) represent the physics of the problem very well.

The correspondence between the experiment and the simulation is not complete, mainly because the initial vortex in the laboratory is slightly affected by the ridge when it is created, in contrast with the initial condition in the numerical case, which is exactly circular. Taking into account that the flow evolution in the vortex–ridge problem is very complicated, however, it is worth emphasizing that the qualitative agreement shown in previous figures is an important result for validating the general

model. As expected, when the simulation is repeated in the absence of Ekman terms, the numerical result (not shown here) differs strongly from the experiment (Zavala Sansón 2001).

4. Final remarks

A general two-dimensional model for rotating barotropic flows over variable topography, together with Ekman effects, was derived. From this formulation some other two-dimensional models can be recovered, for instance the barotropic non-divergent equations, (2.26)–(2.29) (see e.g. Grimshaw *et al.* 1994), or the model with Ekman friction over a flat bottom, (2.30)–(2.33), developed in ZH00 (see also Zavala Sansón *et al.* 2001). The extended model can also be applied to flows over a flat bottom and a spatially variable surface. Its main characteristic is the inclusion of nonlinear Ekman terms in the vorticity evolution equation, in addition to the well-known linear damping term. Another difference with conventional formulations is that Ekman terms in (2.20) contain the x, y-dependent factor $1/h(x, y)$. In contrast, for a flat bottom and for the quasi-geostrophic regime (i.e. with small depth variations), this factor is constant.

It should be mentioned that the linear Ekman condition (2.6) is used as the lower boundary condition. This assumption, however, is only strictly valid for low-Rossby-number flow, $\epsilon = \omega/f \ll 1$. Therefore the pumping from the Ekman layer should be proportional to $\omega + O(\epsilon)$ instead of just ω (plus topographic terms). As explained in ZH00, the 'extra' vertical velocity is not taken into account in the present approximation. The justification for using this procedure is empirical, since laboratory experiments can be simulated very effectively. Furthermore, this condition allows a relatively simple formulation of bottom viscous effects, which facilitates their analytical and numerical treatment and, more importantly, their physical interpretation.

The general model was tested by considering the experimentally observed evolution of an isolated vortex under the influence of the parabolic free surface in a rotating tank (Vosbeek 1998). In this case, the vortex evolves into a tripolar structure approaching the centre of the tank. Qualitative and quantitative experimental observations were compared with numerical simulations based on the general model, namely the evolution of vorticity contours and the peak vorticity decay at the vortex core during more than an Ekman period. The results strongly suggest that such a two-dimensional formulation incorporates both inviscid and viscous topography effects correctly. A similar procedure was applied to study the flow due to a non-isolated sink vortex over a topographic ridge (a more complete description is found in Zavala Sansón 2002). Good qualitative agreement between the experiment and simulation was found even for times comparable with the Ekman timescale. This is an important result since topographic changes are much more dramatic in the ridge experiment than in the γ-plane. For instance, depth variations due to the ridge are of order $h_B/H \approx 3/21 \approx 0.14$, while on the parabolic surface the depth variations are only $h_B/H \approx 0.3/16 \approx 0.02$.

Discrepancies between experiments and simulations can be attributed to the unavoidable differences in the initial conditions. Furthermore, the model does not take into account the time-dependent free-surface deformations associated with the flow. Additional studies with more complicated topographies and initial vorticity distributions would be necessary in order to further affirm the validity of the model. It must also be mentioned that this approximation clearly seems to be superior to the

conventional quasi-geostrophic approximation (for the present flow regimes) and to the inviscid model with variable topography. Conventional models are still useful when studying the flow evolution during times shorter than the Ekman timescale. For times comparable to or longer than the Ekman period, however, the present formulation should be applied.

L. Z. S. gratefully acknowledges financial support from the Consejo Nacional de Ciencia y Tecnología (CONACYT, México) and from Eindhoven University of Technology (TUE, The Netherlands) during the early preparation of this paper.

REFERENCES

Carnevale, G. F., Kloosterziel, R. C. & van Heijst, G. J. F. 1991 Propagation of barotropic vortices over topography in a rotating tank. *J. Fluid Mech.* **233**, 119–139.

Charney, J. G. & Eliassen, A. 1949 A numerical method for predicting the perturbations of the middle-latitude westerlies. *Tellus* **1**, 38–54.

van Geffen, J. H. G. M. 1998 *NS-evol*. Internal report R-1466-D, Fluid Dynamics Laboratory, Department of Physics, Eindhoven University of Technology, The Netherlands.

Gill, A. E. 1982 *Atmosphere–Ocean Dynamics*. Academic Press.

Grimshaw, R., Tang, Y. & Broutman, D. 1994 The effect of vortex stretching on the evolution of barotropic eddies over a topographic slope. *Geophys. Astrophys. Fluid Dyn.* **76**, 43–71.

Hart, J. E. 1995 Nonlinear Ekman suction and ageostrophic effects in rapidly rotating flows. *Geophys. Astrophys. Fluid Dyn.* **79**, 201–222.

Hart, J. E. 2000 A note on nonlinear corrections to the Ekman layer pumping velocity. *Phys. Fluids* **12**, 131–1135.

van Heijst, G. J. F. 1994 Topography effects on vortices in a rotating fluid. *Meccanica* **29**, 431–451.

van Heijst, G. J. F., Kloosterziel, R. C. & Williams, C. W. M. 1991 Laboratory experiments on the tripolar vortex in a rotating fluid. *J. Fluid Mech.* **225**, 301–331.

Hopfinger, E. J. & van Heijst, G. J. F. 1993 Vortices in rotating fluids. *Annu. Rev. Fluid Mech.* **25**, 241–289.

Huppert, H. E. & Bryan, K. 1976 Topographically generated eddies. *Deep-Sea Res.* **23**, 655–679.

Kloosterziel, R. C. & van Heijst, G. J. F. 1992 The evolution of stable barotropic vortices in a rotating free-surface fluid. *J. Fluid Mech.* **239**, 607–629.

Maas, L. R. 1993 Nonlinear and free-surface effects on the spin-down of barotropic axisymmetric vortices. *J. Fluid Mech.* **246**, 117–141.

Orlandi, P. & van Heijst, G. J. F. 1992 Numerical simulation of tripolar vortices in two-dimensional flow. *Fluid Dyn. Res.* **9**, 179–206.

Pedlosky, J. 1987 *Geophysical Fluid Dynamics*. Springer.

Taylor, G. I. 1923 Experiments on the motion of solid bodies in rotating fluids. *Proc. R. Soc. Lond.* A **104**, 213–218.

Velasco Fuentes, O. U., van Heijst, G. J. F. & Lipzig, N. P. M. 1996 Unsteady behaviour of a topography-modulated tripole. *J. Fluid Mech.* **307**, 11–41.

Vosbeek, P. W. C. 1998 Contour dynamics and applications to two-dimensional vortices. PhD thesis, Eindhoven University of Technology.

Wedemeyer, E. H. 1964 The unsteady flow within a spinning cylinder. *J. Fluid Mech.* **20**, 383–399.

Zavala Sansón, L. 2002 Vortex-ridge interaction in a rotating fluid. *Dyn. Atmos. Oceans* (in press).

Zavala Sansón, L. & van Heijst, G. J. F. 2000*a* Nonlinear Ekman effects in rotating barotropic flows. *J. Fluid Mech.* **412**, 75–91 (referred to herein as ZH00).

Zavala Sansón, L. & van Heijst, G. J. F. 2000*b*. Interaction of barotropic vortices with coastal topographies: Laboratory experiments and numerical simulations. *J. Phys. Oceanogr.* **30**, 2141–2162.

Zavala Sansón, L., van Heijst, G. J. F. & Backx, N. A. 2001 Ekman decay of a dipolar vortex in a rotating fluid. *Phys. Fluids* **13**, 440–451.